Journal of Materials Chemistry C

ROYAL SOCIETY OF CHEMISTRY

PAPER

View Article Online
View Journal | View Issue

Check for updates

Cite this: J. Mater. Chem. C, 2025, 13, 10310

A low-power filamentary memristor crossbar array enabled *via* cubic α-phase stabilized mixed-cation lead halide perovskites†

In Hyuk Im,‡[a] Ji Hyun Baek,‡[a] Do Yeon Heo,‡[bc] Sung Hyuk Park,[a] Sohyeon Park,[a] Seung Ju Kim,[ad] Jae Young Kim,[a] Youngmin Kim,[a] Yoon Jung Lee,[ae] Kyung Ju Kwak,[a] Hyeon Ji Lee,[a] Soo Young Kim *[b] and Ho Won Jang *[af]

Halide perovskite (HP)-based resistive switching memory has demonstrated significant advantages, particularly in terms of rapid switching speed and low power consumption. To address the thermal instability associated with $CH_3NH_3^+$ ions, which have been mainly focused on in related fields, we developed resistive switching memory utilizing distorted HPs ($FA_{0.8}Cs_{0.2}PbI_3$), incorporating thermally stable A-site cations. Moreover, we improved nonvolatility by introducing SCN anions to stabilize the cubic α-phase. Unlike the pristine $FACsPbI_3$ (FCPI) device untreated by the SCN^--based additive, which features an α-phase/δ-phase heterostructure and exhibits unstable switching characteristics, the FCPI-SCN device demonstrates a stable cubic α-phase and extended retention behavior. After α-phase stabilization, trap-controlled emission becomes dominant in the FCPI-SCN device, confirming the stable filament formation through the HP layer. This strategic approach effectively suppresses the formation of heterostructures, reducing planar defects that serve as preferential sites for the multiple thin filament formation, thereby promoting stable filaments within the matrix. While pristine FCPI exhibits an unstable retention time of 40 s, FCPI-SCN demonstrates significantly improved performance including low operating voltages of 0.248 V/−0.116 V, a prolonged retention time of 11 000 s, and endurance over 1200 cycles. Additionally, we fabricated a 3 × 3 crossbar array with FCPI-SCN filamentary memristor devices. The crossbar array efficiently encodes and preserves letter-based bitmaps, thus showcasing its practical utility for reliable nonvolatile memory applications.

Received 22nd January 2025,
Accepted 6th April 2025

DOI: 10.1039/d5tc00303b

rsc.li/materials-c

Open Access Article. Published on 10 April 2025. Downloaded on 8/1/2025 4:22:04 PM.
This article is licensed under a Creative Commons Attribution-NonCommercial 3.0 Unported Licence.

Introduction

Conventional memory technologies have confronted a significant challenge known as the 'memory wall,' an inherent limitation in the von Neumann structure.[1,2] This bottleneck is exacerbated by the exponential growth of data, which leads to increased latency across the entire von Neumann-based computing system. Consequently, it becomes imperative to establish a bridge between these hierarchical components.[3–7] In the last decade, there has been a growing demand for novel emerging memory technologies, commonly referred to as memristors. This is due to their advantages, including ease of cell integration, enhanced energy efficiency, and outstanding performance in both memory and neuromorphic applications.[8–10] While the exploration of resistive switching behaviors has predominantly revolved around various oxide-based materials,[11–14] there are still limitations related to mechanical flexibility and reduced binding energy, which are critical for biomimetics and low-power consumption. These underscore the pressing need for the discovery of more advanced materials.

Inorganic–organic halide perovskites (HPs) have garnered significant attention owing to their notable advantages, encompassing a tunable bandgap, controllable majority carriers, rapid ion migration, and remarkable flexibility.[15–18] Of particular significance, HPs have demonstrated substantial potential in resistive random-access memory applications, demonstrating

[a] Department of Materials Science and Engineering, Research Institute of Advanced Materials, Seoul National University, Seoul, 08826, Republic of Korea. E-mail: hwjang@snu.ac.kr
[b] Department of Materials Science and Engineering, Korea University, Seoul, 02841, Republic of Korea. E-mail: sooyoungkim@korea.ac.kr
[c] Hydrogen Ion Materials Group, National Institute for Materials Science, Tsukuba, 305-0044, Japan
[d] Department of Electrical and Computer Engineering, University of Southern California, Los Angeles, CA 90089, USA
[e] School of Electrical Engineering, Kookmin University, Seoul 02707, South Korea
[f] Advanced Institute of Convergence Technology, Seoul National University, Suwon 16229, Republic of Korea

† Electronic supplementary information (ESI) available. See DOI: https://doi.org/10.1039/d5tc00303b

‡ I. H. Im, J. H. Baek and D. Y. Heo contributed equally to this work.

This journal is © The Royal Society of Chemistry 2025

Open Access Article. Published on 10 April 2025. Downloaded on 8/1/2025 4:22:04 PM.
This article is licensed under a Creative Commons Attribution-NonCommercial 3.0 Unported Licence.

ultralow operating voltages and high on–off ratios which are based on their soft and flexible bonding matrix. Our previous works have reported on HP-based electrochemical metallization memory and artificial synaptic devices operating at ultralow voltage.[19–23] This characteristic stems from the low activation energy barrier for the movement of vacancies and ions in the halide matrix. Besides, previous studies have demonstrated that HPs composed of Ag exhibit resistive switching behavior by preformed conductive filaments, with low operating voltages and high on/off ratio.[19] Ag atoms can readily move within the HP matrix under an electric field, contributing to the efficient performance of the devices.

Among the various HPs, $CH_3NH_3PbI_3$ ($MAPbI_3$) has been the subject of extensive research.[24,25] However, the thermal instability of the methylammonium ($CH_3NH_3^+$, MA^+) cation, which tends to decompose into CH_3I and NH_3^+, poses a significant challenge.[26,27] To address this issue, a mixed-cation approach involving formamidinium ($HC(NH_2)_2^+$, FA^+) and Cs^+ cations has been pursued.[28,29] The FA cation has demonstrated promise due to its enhanced thermal stability,[30,31] remaining intact within the temperature range of 100 to 175 °C.[32] Furthermore, the inorganic Cs cation provides enhanced long-term stability compared to its organic counterparts.[26] By integrating a mixed-cation composition ($FA_{1-x}Cs_xPbI_3$), as illustrated in Fig. 1(a), endeavors have been made to engineer a distorted perovskite structure, which has tilted octahedra, thereby optimizing the Goldschmidt tolerance factor.[33] Despite these advancements, FA-based HPs have faced challenges concerning the susceptibility of the black α-phase perovskites and their transition to the yellow δ-phase non-perovskites, primarily located at the grain boundary and characterized by a high density of defects.[34,35] Notably, it has been established that the formation of the conductive filament is intrinsically associated with planar defective sites, such as grain boundaries and interfaces, and their modulation is crucial for achieving reliable switching operations.[36,37] Interface engineering plays a critical role in controlling the resistive switching behaviour of halide perovskite-based memristors.[38–40] Previous studies have highlighted the significant influence of the interface on the filamentary switching mechanism. In this respect, the heterostructure induced by phase instability may lead to irreversible switching behavior. Furthermore, the α-phase exhibits a one-dimensional (1D)-like channel, where corner-shared PbI_6 octahedra align linearly, facilitating the migration of constituent ions.[41–43] This structural attribute is essential for generating the *I–V* hysteresis behavior in HP-based resistive switching devices.

This study delves into the stabilization of the cubic α-phase in HP-based filamentary memristor devices through the introduction of thiocyanate (SCN) anions. The SCN anion, a pseudohalide ion, possesses an ionic radius (2.15–2.20 Å) similar to that of the iodine (I^-) ion. Incorporation of SCN anions into HPs has shown an enhancement in both crystallinity and electronic properties.[44–48] Our focus was on the $FA_{0.8}Cs_{0.2}PbI_3$ distorted perovskites, known for their stable composition conducive to the cubic phase.[49] In this endeavor, we strategically employed SCN treatment during the film deposition process. In the absence of SCN^--based additive treatment, the pristine $FACsPbI_3$ (FCPI) film exhibited a mixture of α and δ-phases, resulting in α/δ-phase heterostructures. The electrons injected mainly into these α/δ-phase heterostructures may lead to the electrochemical reduction of migrating Ag cations within the HPs. Multiple thin filaments are mainly generated along the heterostructures, possessing enlarged effective surface curvature for each filament. The tendency to minimize surface energy drives the surface atom diffusion of the filaments. Therefore, the geometry of the filaments is critical in surface diffusion circumstances. The increased surface curvature of the thin filaments renders them vulnerable to surface atom diffusion. Consequently, fast surface diffusion of thin filaments leads to an unfavorable nonvolatile characteristic. Conversely, the incorporation of SCN anions contributed to enhanced stability of the black α-phase perovskite within the FCPI system, thereby promoting the formation of filaments through the halide matrix. In the SCN^--mediated $FACsPbI_3$ (FCPI-SCN), space-charge limited conduction (SCLC) was observed in the high-resistance state (HRS), unlike the pristine case. This bulk-limited conduction suggests that the HRS current is dependent on trap-controlled emission by the charged ions that are distributed in cubic α-phase HPs. Subsequently, electrochemically dissolved Ag cations interact with carriers transferred between charged ions to recrystallize, thereby enabling the transition to the low-resistance state (LRS). This indicates that stable Ag filament formation occurs through the α-phase stabilized FCPI-SCN layer, resulting in the reduction of filament surface curvature and slow surface atom diffusion. The FCPI-SCN device showcased enhanced device performances, including low operating voltages, fast switching speed, extended retention time, improved endurance, and a heightened multilevel capability compared to its pristine counterpart. Additionally, a 3 × 3 crossbar array utilizing FCPI-SCN was constructed and evaluated for its capability to store and retrieve bitmap images representing the acronym of our laboratory: 'O,' 'N,' 'N,' and 'L.'

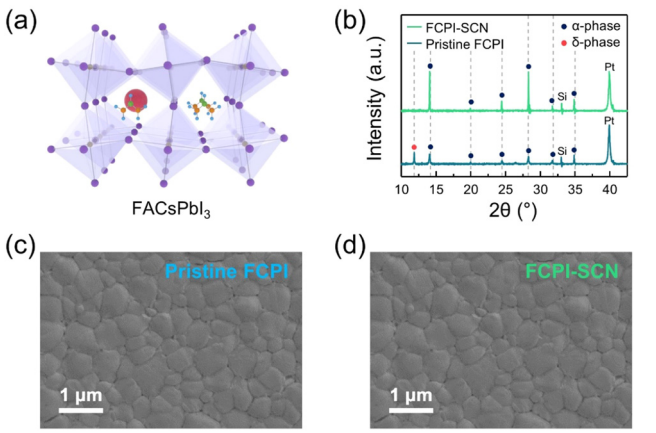

Fig. 1 Distorted halide perovskites of $FACsPbI_3$ treated with an SCN^--based additive. (a) The schematic of the crystal structure of the distorted halide perovskite $FA_{0.8}Cs_{0.2}PbI_3$. (b) The XRD patterns of the pristine FCPI and FCPI-SCN, showing the stabilization of the cubic α-phase by SCN^- treatment. The top view SEM image of (c) the pristine FCPI and (d) FCPI-SCN.

Open Access Article. Published on 10 April 2025. Downloaded on 8/1/2025 4:22:04 PM. This article is licensed under a Creative Commons Attribution-NonCommercial 3.0 Unported Licence.

The crossbar array reliably retained all bitmaps. This work elucidates the correlation between filamentary switching mechanisms and the matrix environment. Furthermore, the enhancement of nonvolatile switching characteristics in the FCPI-based low-powered switching device underscores the potential of halide perovskite-based conductive bridge random access memory (CBRAM) for storage-class memory applications.

Experimental

Materials preparation

Formamidinium iodide ($(HC(NH_2)_2I$, 99.99%) was purchased from GreatCellSolar Materials. Cesium iodide (CsI, 99.9%), ammonium thiocyanate (NH_4SCN, 99.99%), *N*,*N*-dimethylformamide (DMF, 99.8%, anhydrous), and dimethyl sulfoxide (DMSO, anhydrous, ≥99.9%) were purchased from Sigma-Aldrich. Lead iodide (PbI_2, 99.99%) and PMMA were purchased from Tokyo Chemical Industry (TCI).

Preparation of FCPI HPs

The FCPI precursor solution was prepared by 0.8 M FAI, 0.2 M CsI, and 1 M PbI_2 powders in 1 mL mixed solvent of DMSO and DMF (1 : 3 v/v). To prepare the FCPI-SCN film, ammonium thiocyanate (NH_4SCN) was added to the FCPI precursor solution at a concentration of 0.2 M, corresponding to 0.0002 mol of NH_4SCN per 1 mL of precursor solution.

Device fabrication

Pt (100 nm)/Ti (20 nm) was deposited on SiO_2//Si substrates for bottom electrodes (BEs) *via* an electron beam (E-beam) evaporation method. The Pt/Ti/SiO_2/Si substrates were cleaned with acetone, isopropanol, and deionized water. Then, they were treated with UV ozone. The FCPI precursors were spin-coated onto the Pt/Ti/SiO_2/Si substrates at 4000 rpm for 60 s, and toluene was dropped after 8 s while spin coating. The films were heated at 180 °C for 10 min. Then, poly(methyl methacrylate) (PMMA) in chlorobenzene with the concentration of 5 mg ml^{-1} was spin-coated at 4000 rpm for 30 s. The films were heated at 180 °C for 3 min. Finally, 50 × 50 μm^2 Ag top electrodes (TEs) were deposited onto the pristine FCPI and FCPI-SCN films *via* E-beam evaporation with a shadow mask.

For comparison, Bi film of 100 nm thickness was deposited on an electropolished Cu foil by an E-beam evaporator at the deposition rate of 0.3 Å s^{-1}. The base pressure of the vacuum chamber was 1.5×10^{-6} Torr.

Fabrication of a crossbar array

Three Pt bottom line electrodes were patterned *via* photolithography (NanoSystem Solutions Inc. DL-1000 HP system). A Pt layer was deposited *via* E-beam evaporation on a patterned resist and a lift-off process was done. FCPI precursors were spin-coated onto the substrate with Pt bottom line electrodes. Then, a PMMA layer was spin-coated. Finally, three Ag line electrodes were deposited by E-beam evaporation with a line-patterned shadow mask of 100 μm width.

Material characterization

The top-view and cross-sectional view images of the FCPI films were obtained using a field-emission scanning electron microscope (SEM) (ZEISS, MERLIN Compact) with an in-lens secondary electron detector which was operated at an accelerating voltage of 3 kV. XRD patterns were obtained with an X-ray diffractometer (BRUKER MILLER Co., D8-Advance) at room temperature with Cu-Kα radiation (λ = 1.54056 Å). X-ray diffraction (XRD) measurements were conducted with a step size of 0.02° and a scanning speed of 5° min^{-1}. Topological images and current mapping of the FCPI films were obtained using atomic force microscopy (AFM) (Park System, NX-10). A fluorescence spectrometer (FlouTime 300; PicoQuant) with an excitation laser of 398 nm was used to measure photoluminescence (PL) and time-resolved photoluminescence (TR-PL) spectra in the range from 600 to 900 nm.

Electrochemical characterization

Agilent 4156C and 4200A-SCS semiconductor analyzers and a Tektronix AFG 3021C were used to measure the electrical properties.

Statistical analysis

All data were processed using Microsoft Excel (Microsoft), OriginPro 9.0 (OriginLab Co., Northampton, MA, USA), and MATLAB R2021b (MathWorks). All C-AFM images were analyzed using XEI software (Park System).

Results and discussion

FACsPbI$_3$-based resistive switching devices with thiocyanate treatment

The FCPI thin film was synthesized through a low-temperature solution process. Three precursors (FAI, CsI, and PbI_2) were dissolved in a mixed solvent of DMF and DMSO. For FCPI-SCN, the precursors were dissolved alongside the SCN^--based additive. Subsequently, the resulting solution was spin-coated onto the Pt BE substrate. The Goldschmidt tolerance factor (t), defined by eqn (1), where r_A, r_B, and r_X are the ionic radius of A, B, and X ions respectively, is a conventional parameter used to assess the ABX_3 perovskite structures.

$$t = \frac{(r_A + r_B)}{\sqrt{2} \cdot (r_B + r_X)} \quad (1)$$

Cubic perovskite structures are typically stable when $0.9 < t < 1.0$. Given the ionic radii of FA, Pb, and I as 253 pm, 119 pm, and 220 pm respectively,[50] $FAPbI_3$ has an ideal t value of 0.99. However, the flat shape of the FA cation leads to a larger effective ionic radius, resulting in a higher effective t value.[33] Therefore, the introduction of smaller Cs cations (167 pm) promotes the t value to reach the cubic perovskites range. Consequently, $FAPbI_3$ exhibits an imperfect cubic structure, as shown in Fig. S1 (ESI†). By mixing FA with the smaller Cs cation at a molar ratio of 8 : 2, $FA_{0.8}Cs_{0.2}PbI_3$ achieves a more

 This journal is © The Royal Society of Chemistry 2025

Open Access Article. Published on 10 April 2025. Downloaded on 8/1/2025 4:22:04 PM.
This article is licensed under a Creative Commons Attribution-NonCommercial 3.0 Unported Licence.

stable cubic structure and high crystallinity, attributed to the decrease in the t value. However, as the Cs content increases, the orthorhombic γ-phase becomes more prevalent due to the decrease in t value. Fig. S2 (ESI†) represents the XRD measurements of FCPI HPs that included various SCN^--based additives. Recent research has demonstrated that alkali ions can impede ion migration within HPs and eliminate I–V hysteresis behavior.[51,52] Thus, additives containing alkali ions were not considered. Instead, the NH_4SCN was chosen due to its capability to stabilize the α-phase crystal structure and its facile removal during deposition process.[53] The XRD patterns of the pristine FCPI and FCPI-SCN films are depicted in Fig. 1(b). The diffraction peaks observed at 2θ = 14.1°, 20.0°, 24.5°, 28.3°, 31.7°, 34.9°, and 39.9° are identified as the (100), (110), (111), (200), (210), (211), and (220) planes of the α-phase crystal structure, respectively. Additionally, a peak at 2θ = 11.9° corresponds to the (100) plane of the δ-phase crystal. These results indicate the successful stabilization of the cubic α-phase in HPs through the introduction of SCN anions. The increased peak intensity is attributed to the improved crystallinity observed in the FCPI-SCN film. SEM images of the FCPI and FCPI-SCN films are presented in Fig. 1(c) and (d), respectively. Furthermore, Fig. S3 (ESI†) shows the AFM images for both films. The root mean square (RMS) roughness improved from 27.7 nm in the pristine FCPI film to 23.8 nm in the FCPI-SCN film. This improvement in roughness, in conjunction with the XRD results, signifies enhanced crystallinity and film morphology.

To assess its electronic characteristics, the FCPI films were synthesized on a prefabricated Pt/Ti/SiO_2/Si substrate. Subsequently, a PMMA layer was spin-coated, and Ag TEs were deposited through a 50 μm × 50 μm square patterned metal mask *via* E-beam evaporation, resulting in the Ag TE/PMMA/HPs/Pt BE vertical-stack structure. Fig. S4 (ESI†) shows the optical image of devices fabricated in a sandwich structure with varying electrode sizes of 400 μm^2, 200 μm^2, 100 μm^2, and 50 μm^2. The SEM images in Fig. 2(a) provide the vertical structure of the FCPI-SCN device, with a FCPI thickness of 400 nm. Fig. 2(b) presents the I–V behavior of the FCPI-SCN device, with the compliance current (I_{cc}) set to 10^{-3} A. A formation process was required at +1.24 V to initially switch from a high resistance state (HRS) to a low resistance state (LRS). The resistance was then switched back to HRS by applying an electric field with negative polarity. Subsequently, DC sweeps were conducted in the sequence 0 V → 0.8 V → −0.8 V → 0 V. During these sweeps, the SET voltage (V_{SET}), where HRS is converted to LRS, was observed around +0.3 V. The RESET voltage (V_{RESET}), where the resistance returns back to HRS, was exhibited around −0.1 V. As shown in Fig. 2(c), the HRS and LRS retention properties of both devices were evaluated by applying a pulse train of read voltage (+0.02 V). The FCPI-SCN device exhibited an impressive retention time of up to 1.1×10^4 s. The resistive switching mechanism of our devices is based on electrochemical metallization, typically observed in devices with electrochemically active Ag electrodes.[54] The electrochemical metallization mechanism involves the following reaction steps. (i) Anodic dissolution: $Ag \rightarrow Ag^+ + e^-$, (ii) migration of Ag cations across the solid–electrolyte, and (iii) reduction and crystallization: $Ag^+ + e^- \rightarrow Ag$. Fig. S5a and b (ESI†) showcase the I–V results of Pt/PMMA/FCPI-SCN/Pt and Pt/PMMA/pristine FCPI/Pt devices, respectively, indicating that Ag metal electrodes show the important resistive switching phenomenon in the FCPI-SCN devices, as no resistive switching

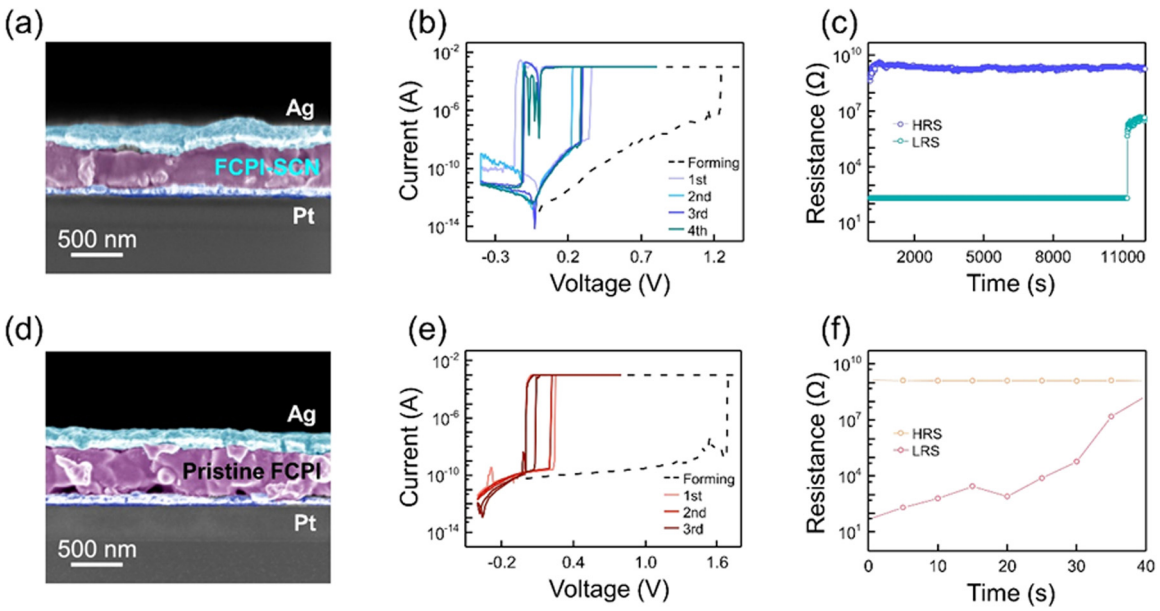

Fig. 2 Comparison of electrical properties between the FCPI-SCN and the pristine FCPI devices. (a) The cross-sectional SEM image of the vertical stack of Ag/PMMA/FCPI-SCN/Pt. The thickness of the FCPI-SCN film is 400 nm. (b) Series of I–V behavior and (c) HRS and LRS retention properties for the FCPI-SCN device. Retention time was measured under a pulse train of the +0.02 V read pulses. (d) The cross-sectional SEM image of the vertical stack of Ag/PMMA/pristine FCPI/Pt. (e) Series of I–V behavior and (f) retention properties for the pristine FCPI device.

Open Access Article. Published on 10 April 2025. Downloaded on 8/1/2025 4:22:04 PM.
This article is licensed under a Creative Commons Attribution-NonCommercial 3.0 Unported Licence.

response was observed when an inert metal TE was used instead of the Ag TE. Fig. S6 (ESI†) illustrates the electrode size dependence of the V_{SET}, V_{RESET}, HRS current, and LRS current in the FCPI-SCN devices with varying electrode sizes, ranging from $(50\ \mu m)^2$ to $(400\ \mu m)^2$. V_{SET} and V_{RESET} remained consistent regardless of the electrode size. These findings indicate that the resistance change in our devices is driven by filamentary switching, which is independent of the electrode area.[55–57] The vertical stack of Ag TE/PMMA/pristine FCPI/Pt is shown in Fig. 2(d). In contrast to the prior case, it displayed different aspects of V_{SET} around +0.25 V and V_{RESET} near 0 V (Fig. 2(e)). As displayed in Fig. 2(f), the pristine FCPI device demonstrated an unstable retention time of 40 s. The pristine FCPI device exhibited unstable switching performance similar to volatile threshold switching devices, which are known for their temporary filament characteristics. In contrast, the FCPI-SCN device demonstrated stable nonvolatile switching performance. These results underscore the significantly enhanced nonvolatile characteristics of the SCN^--mediated case compared to the pristine case.

Detailed observation of the switching behavior of $FACsPbI_3$ devices

Fig. 3(a) presents the replotted *I–V* characteristics of the FCPI-SCN device on a double-logarithm scale. Prior to the SET process, current conduction in HRS is governed by classical trap-controlled SCLC, which comprises three distinct mechanisms:[58–60] the ohmic conduction region ($I \propto V$), the trap-unfilled SCLC region adhering to the Mott–Gurney law ($I \propto V^2$), and the trap-filled SCLC region characterized by a steep current increase. After the SET process, ohmic conduction, which is identified by a linear slope with a gradient of approximately 1 on a double-logarithmic scale, becomes predominant. Analysis of three portions in the HRS is depicted in Fig. 3(b)–(d). Initially, upon the application of the electric field, ohmic conduction, indicated by a linear slope with a gradient of approximately 1 on a double-logarithmic scale, prevails in the Ag/PMMA/FCPI-SCN/Pt device (Fig. 3(b)). Subsequently, the current conduction transitions to the trap-unfilled SCLC mechanism, demonstrated by a slope of 2 on a double-logarithmic scale (Fig. 3(c)). This shift is attributed to the low activation energy for the electrically induced generation of halide vacancies in cubic α-phase halide perovskites.[33] As shown in Fig. 3(d), at higher electric fields, the current is governed by the trap-filled space-charge limited conduction (SCLC), characterized by a steep slope of 3.4 on a double-logarithmic scale. The trapping centers for electron conduction are likely attributed to migrated Ag cations. Upon reaching V_{SET}, the reduction of Ag and electrocrystallization of the filament occur, making the overall resistance dependent on the contact between the electrode and the metallic filaments.

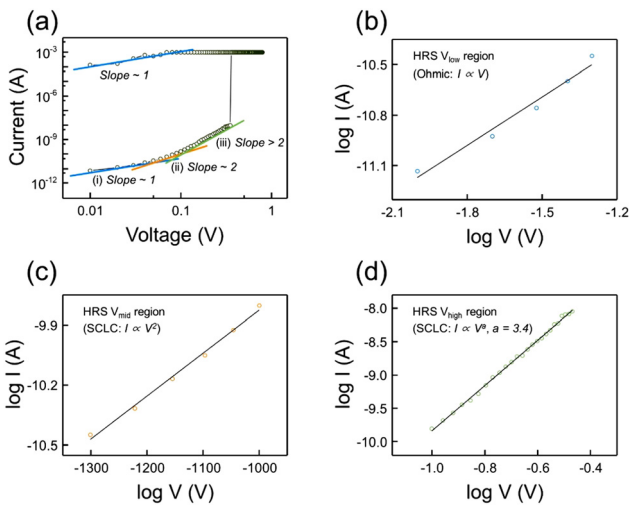

Fig. 3 Analysis of conduction mechanisms in the FCPI-SCN device. (a) Double logarithmic plots of *I–V* curves of the FCPI-SCN devices. Current conduction in HRS comprises the ohmic conduction with a slope of 1, the trap-unfilled SCLC with a slope of 2, and the trap-filled SCLC with a steep current increase. (b) The ohmic conduction region ($I \propto V$). (c) The trap-unfilled SCLC region adhering to the Mott–Gurney law ($I \propto V^2$). (d) The trap-filled SCLC region ($I \propto V^a$, a = 3.4).

These results suggest that in the FCPI-SCN device, the initial stage of current conduction is influenced by the ohmic interface between the electrode and cubic α-phase FCPI-SCN. As the external field increases, halide vacancies are released due to the low formation energy of Frenkel defects of iodine (V_I^+: positive iodine vacancy/I_I^-: negative interstitial iodine) in the cubic α-phase HPs.[43,61,62] Consequently, these charged sites induce SCLC conduction in the FCPI-SCN device.[63] At the higher field region, traps are filled by more injected carriers, leading to trap-filled SCLC. When the field reaches V_{SET}, the electrochemically dissolved Ag cations react with carriers transferred through cubic α-phase HPs by SCLC. Consequently, the crystallization of Ag occurs and metal filaments are formed through the cubic α-phase HP film.

In contrast, the pristine FCPI device exhibits a different current conduction mechanism. Fig. S7a (ESI†) shows replotted *I–V* graphs of the pristine FCPI device in a double-logarithm scale. Fig. S7b and c (ESI†) represent replotted graphs for HRS and LRS of the pristine FCPI device, respectively. As shown in Fig. S7b (ESI†), the intrinsic conduction in the HRS is primarily governed by Schottky emission ($\ln I \propto V^{1/2}$) and is observed prior to the SET process. It is attributed to the formation of the hexagonal δ-phase that possesses a higher bandgap compared to the cubic α-phase in the pristine FCPI device.[64] The hexagonal δ-phase is mainly observed at the grain boundaries and interfaces cubic α-phase HPs.[65,66] Before the filament is generated, the current is primarily influenced by the interfaces between the hexagonal δ-phase and electrodes. At the V_{SET} value, the conduction mechanism in LRS is dominated by the ohmic conduction due to the formation of Ag filaments, as represented in Fig. S7c (ESI†).

Unlike the FCPI-SCN case, current conduction across the entire HRS range of the pristine FCPI device is governed by the Schottky emission, which arises from the interfaces between the hexagonal δ-phase and the electrodes. The electrochemical reaction of dissolved Ag is likely predominantly influenced by the carriers transferred through the hexagonal δ-phase. The TR-PL spectra of the pristine FCPI and FCPI-SCN films are shown

 This journal is © The Royal Society of Chemistry 2025

Open Access Article. Published on 10 April 2025. Downloaded on 8/1/2025 4:22:04 PM.
This article is licensed under a Creative Commons Attribution-NonCommercial 3.0 Unported Licence.

in Fig. S8 (ESI†). The FCPI-SCN film exhibits longer carrier lifetime values (τ_2) of 26.2 ns, compared to the pristine FCPI film displaying 14.1 ns. The values are fitted by a bi-exponential function for the PL decay kinetics: $A_1 \cdot \exp(-t/\tau_1) + A_2 \cdot \exp(-t/\tau_2)$.[67] Decreased carrier lifetime arises from coexistence with the hexagonal δ-phases in the FCPI film, which are known for being photo-inactive and defective non-perovskite phases.[45,68,69] The planar defects indeed play a pivotal role as preferential pathways for generating conductive filaments due to variations in local electrical field strength.[36,37,70] In the pristine FCPI device, electrons injected mainly into these α/δ-phase heterostructures participate in the electrochemical reduction of dissolved Ag cations. Hence, the heterointerfaces in the pristine FCPI facilitate the formation of numerous dendritic thin filaments within the HP layer.

Stable filament formation in SCN^--mediated $FACsPbI_3$

The filamentary switching behavior of both the FCPI-SCN and pristine devices was visualized using conductive atomic force microscopy (C-AFM). Thin films were deposited on an Ag/Ti/SiO_2/Si substrate and scanned with a biased tip while grounding the Ag BE. Fig. 4(a) and (b) illustrate the current mapping of the FCPI-SCN device during the initial 1 V scan and a subsequent 5 V scan, respectively. A distinct and localized current change is observed due to filamentary switching during the subsequent scan. The pristine FCPI device was scanned under identical conditions, as shown in Fig. 4(c) and (d). The filamentary regions in the pristine FCPI device were more dispersed, indicating that the conductive channels in the pristine FCPI were generated in a more distributed manner.

Metal filaments in the solid–electrolyte are significantly influenced by the interfacial energy-related Gibbs–Thomson effect, which describes the structural evolution to minimize system energy, analogous to how a dropping cylinder of fluid splits into several spherical droplets.[71,72] The driving force to minimize the surface energy triggers surface diffusion of the filaments, which can be described using eqn (2):

$$J_s = -\left(\frac{D_s \gamma \delta^4}{kT}\right) \nabla_s \kappa \quad (2)$$

where J_s is the surface atomic flux, D_s is the surface diffusion coefficient, γ is the surface energy, δ is the interatomic distance, κ is the surface curvature ($\kappa = 1/r_1 + 1/r_2$, where r_1 and r_2 are the principal radii of the curvature), k is Boltzmann's constant, and T is the temperature. The surface flux (J_s) escalates with the increase of the surface curvature ($1/r$). In other words, eqn (2) indicates that surface diffusion within the conductive filament is strongly dependent on its radius r. Recent studies have reported that the relaxation kinetics of Ag filaments are governed by a relaxation time t_r proportional to r^4 ($t_r \propto r^4$).[73] It can be deduced that relatively fast transition of the resistance observed in pristine FCPI is attributable to the fast diffusion of filaments with a smaller radius, as evidenced by the dispersed distribution of conductive points in the current mapping. Accordingly, the aspects of the filament formation can be described in two ways.

As illustrated in Fig. 5(a), the distributed events of the filaments in the pristine FCPI device leads to the formation of multiple Ag thin filaments along heterointerfaces. It is hypothesized that filament formation in pristine FCPI primarily occurs at the heterointerfaces between the α- and δ-phases. Consequently, the large effective surface curvature ($1/r$) of the thin filaments accelerates their electrochemical corrosion due to a fast surface diffusion, ultimately resulting in detrimental nonvolatile characteristics. However, in the SCN-treated case, strong interaction between SCN^- and Pb^{2+} ions is attributed to its lone pairs of electrons due to the linear molecular shape of

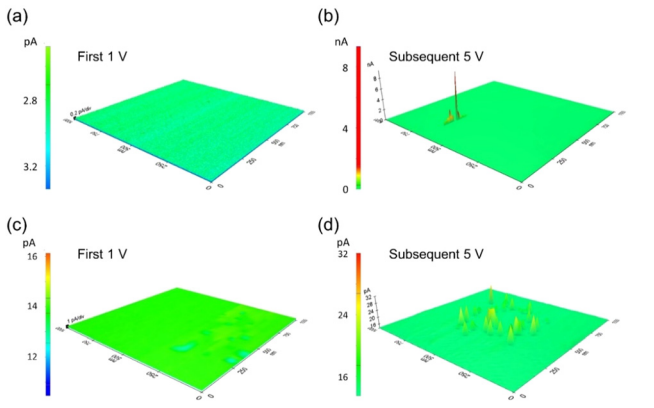

Fig. 4 C-AFM measurement for the filamentary switching region of FCPI-SCN and pristine FCPI on the Ag/Ti/SiO_2/Si substrate. Current mapping of (a) and (b) FCPI-SCN/Ag/Ti/SiO_2/Si and (c) and (d) pristine FCPI/Ag/Ti/SiO_2/Si device with C-AFM. The current was measured by applying 1 V during the first scan (a) and c), followed by subsequent scans at 5 V (b) and (d).

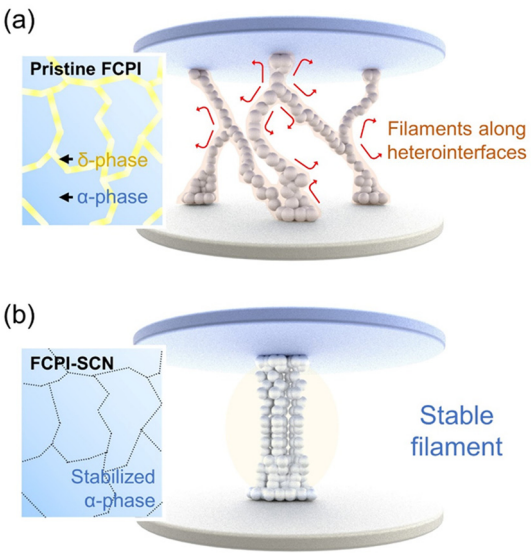

Fig. 5 Filament corrosion in the pristine FCPI device and the stable filament formation in the α-phase stabilized FCPI-SCN devices. (a) Multiple dendritic filaments formation along the heterostructure (α and δ-phases) of the pristine FCPI device, triggering their corrosion due to fast surface diffusion. (b) Enhanced nonvolatile filament in the FCPI-SCN device by the inhibition of δ-phase formation and the α-phase stabilization.

Open Access Article. Published on 10 April 2025. Downloaded on 8/1/2025 4:22:04 PM.
This article is licensed under a Creative Commons Attribution-NonCommercial 3.0 Unported Licence.

the SCN anion, in contrast to the spherical I anion.[47] This interaction facilitates the formation of $Pb(SCN)_4^{2-}$ octahedra, which possess a higher formation constant (K_4) compared to PbI_4^{2-} octahedra.[74] As a result of these interactions, the heterostructure is prevented, thereby stabilizing the α-phase within the FCPI-SCN film. As aforementioned, the metallization of Ag occurs *via* electrochemical reaction by carriers transferred through the HP matrix. This leads to the formation of stable filaments through the FCPI-SCN film, thereby curtailing the effective surface curvature of the filament, as depicted in Fig. 5(b). Consequently, the FCPI-SCN device manifests improved nonvolatile characteristics.

Stable filament formation in SCN^--mediated $FACsPbI_3$

In Fig. 6(a), the resistance distribution of LRS and HRS across 50 distinct cells in the FCPI-SCN device is depicted. It demonstrates a remarkable on/off ratio, with an average value of 4.46×10^8. Additionally, the statistical analysis illustrated in Fig. 6(b) presents the statistical distributions of V_{SET} and V_{RESET} across 15 individual FCPI-SCN devices. The average values of V_{SET} and V_{RESET} are 0.248 ± 0.025 V and -0.116 ± 0.011 V, respectively. Notably, the V_{SET} and V_{RESET} distributions exhibit minimal variations. As depicted in Fig. S9, the cumulative percentiles of V_{SET} and V_{RESET} reveal that the average cycle-to-cycle values of the FCPI-SCN devices are 0.242 ± 0.053 V and -0.11 ± 0.017 V, respectively. Furthermore, the FCPI-SCN device remained operable for up to 1200 cycles of ±1 V (50 μs/100 μs pulse durations), followed by a read voltage of +0.02 V, as displayed in Fig. 6(c). Fig. S10 (ESI†) demonstrates that the FCPI-SCN device remained operational for up to 3500 SET/RESET cycles under low-amplitude pulse conditions. This result suggests that reducing the electrical stimulus can improve the cyclability of the device. The observed fluctuation in resistance states is attributed to the relaxation behavior of the Ag filament. During the reset process, residual Ag ions require time to diffuse, and the extent of diffusion can vary from cycle to cycle.[73,75] Therefore, correction techniques such as closed-loop pulse switching (CLPS)[76,77] may be effective in narrowing the distribution of resistance states and enhancing device endurance. Nonvolatile switching devices intrinsically suffer from the "voltage–time dilemma" where the high operation voltage is usually needed for fast switching speed.[78–80] Because this ion mass transport induces the voltage–time dilemma, we optimized the amplitude to promote reading a clear RESET states distribution and provide a large window between LRS and HRS (Fig. 6(c)). Fig. 6(d) showcases the superior range of multilevel resistance states achieved by the FCPI-SCN device. It was subjected to a DC bias sweeping sequence: 0 V → +0.8 V → 0 V → −0.4 V → 0 V with varying I_{cc}s of 10^{-3}, 10^{-4}, 10^{-5}, 10^{-6}, 10^{-7}, and 10^{-8} A. It attained a total of six distinct LRSs. The multilevel retention times were evaluated using a pulse train of the read voltage (+0.02 V), as displayed in Fig. 6(e). Each resistance state persisted for durations exceeding 10^3 s. Despite prior studies indicating that most electrochemical metallization memories exhibit I_{cc}-dependent behavior, characterized by volatile switching at low I_{cc} and nonvolatile switching at high I_{cc} values,[81,82] the FCPI-SCN device upholds its nonvolatile characteristic even at the extremely low I_{cc} value of 10^{-8} A. In addition, the FCPI-SCN device demonstrates a rapid switching speed of under 50 ns, as illustrated in Fig. 6(f). Table 1 tabulates the general properties of several studies on electrometallization memories. This comparison suggests that HP-based memristors possess low

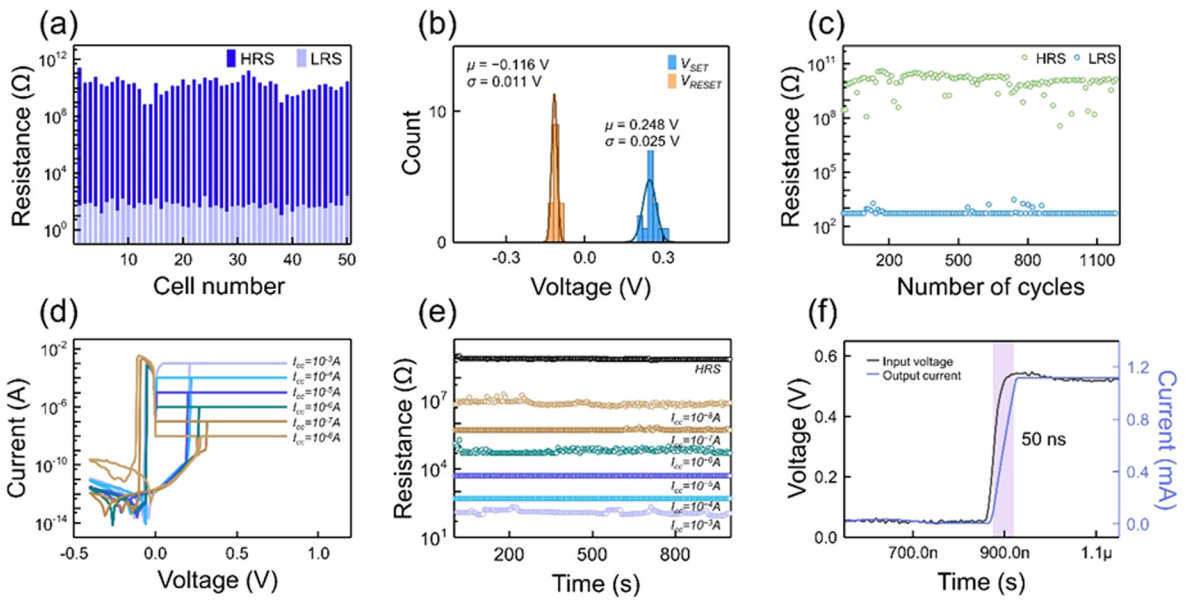

Fig. 6 Nonvolatile switching performances of the FCPI-SCN device. (a) Resistance distribution of LRS and HRS in 50 different cells. (b) The distribution statistics for V_{SET} and V_{RESET}. The symbol μ and σ represent the mean value and the standard deviation, respectively. (c) Endurance test of the FCPI-SCN device. Endurance tests were conducted under pulse train of ±1 V (50 μs/100 μs pulse durations) followed by the read voltage of 0.02 V. (d) Multilevel I–V behavior various with I_{cc}s of 10^{-3}, 10^{-4}, 10^{-5}, 10^{-6}, 10^{-7}, and 10^{-8} A. (e) Multilevel retention times measured by the pulse train of the read voltage (+0.02 V). (f) The switching speed of the FCPI-SCN device measured with input voltage of 0.5 V and base voltage of 0.05 V.

 This journal is © The Royal Society of Chemistry 2025

Open Access Article. Published on 10 April 2025. Downloaded on 8/1/2025 4:22:04 PM. This article is licensed under a Creative Commons Attribution-NonCommercial 3.0 Unported Licence.

Table 1 Performance comparison in the device properties of recently reported electrometallization memories

Memristive materials	Device structure	Set/reset voltage	On/off ratio	Retention time	Endurance	Switching speed	Thickness (nm)	Ref.
Oxides	Ag/ZrO_2/WS_2/Pt	0.2 V/−0.1 V	10^4	4×10^4 s	10^9 cycles	10 ns	100	83
	Ag/VO_x/Pt	0.23 V/−0.07 V	10^3	4×10^4 s	10^3 cycles	—	35	84
	Ag/SiO_2/ITO	3 V/gradual reset	10^2	2×10^3 s	5×10^2 cycles	100 ns	60	85
	Ag/VO_2/SiO_x/n^{++}Si	2.2 V/−2.1 V	60	—	30 cycles	—	—	86
	Ag/$CoFe_2O_4$/Pt	2.5 V/−2.6 V	10^3	10^3	5×10^2 cycles	—	100	87
	Ag/STO/p^{++}-Si	3 V/−1.8 V	10^3	10^4 s	10^3 cycles		70	88
2D materials	Ag/graphdiyne oxide/Au	0.25 V/−0.4 V	10^2	3×10^3 s	1.5×10^2 cycles	—	5	89
	Ag/MoS_2/Ag	0.18 V/−0.1 V	10^7	10^5 s	—	400 ns	100	90
Organic materials	Ag/polyvinyl alcohol–graphene oxide/Ag	0.4 V/−0.8 V	7	3×10^3 s	2.5×10^3 cycles	—	—	91
	Cu/P3HT:PCBM/ITO	4.5 V/−2 V	10^4	10^6 s	—	—	85	92
Halide perovskites	Ag/BA_2PbI_4/Pt	0.5 V/−0.6 V	10^7	10^3 s	2.5×10^2 cycles	10 ms	470	93
	Ag/PMMA/FCPI-SCN/Pt	0.25 V/−0.12 V	10^8	1.1×10^4 s	1.2×10^3 cycles	50 ns	400	This work

operating voltages, fast switching speed, and suitable performances. Fig. S11a (ESI†) displays the XRD patterns, confirming the maintenance of the cubic α-phase after 15 days in an ambient atmosphere. Fig. S11b (ESI†) depicts the stable non-volatile switching characteristics of the treated devices over the same period. Long-term stability was assessed by evaluating device performance after one month of storage under ambient air conditions. The switching performance including retention time and endurance cycles remained stable and reliable, as demonstrated in Fig. S12 (ESI†). These support the effectiveness of SCN treatment in enhancing the reliability of filamentary switching in HP-based devices.

A 3 × 3 crossbar array incorporating the FCPI-SCN device was fabricated to assess its functionality in storing and retrieving bitmap images. The schematic of the crossbar array, constructed on the SiO_2/Si substrate, is illustrated in Fig. 7(a). Fig. 7(b) and Fig. S13 (ESI†) presents an optical image of the 3 × 3 crossbar array with 100 μm-width top and bottom electrode lines. The crossbar array adopted the floating V_r biasing scheme, outlined in Fig. 7(c), whereby all neighboring cells are left floating while the target cell is biased. To validate the storage capability of the FCPI-SCN crossbar array, a 3 × 3-pixel voltage input in the shape of the letter 'X' (depicted in Fig. S14a, ESI†) was programmed into the array. The resulting output current, as illustrated in Fig. S14b (ESI†), successfully converted the programmed data into binary image data. Although the sneak path issue is inevitable (manifested by relatively lower detected current in the SET cell located at the center of the bitmap compared to neighboring SET cells), the readout margin within the 3 × 3 crossbar array remains acceptable. This margin was calculated using the Kirchhoff equation and meets the criterion of a 10% readout margin (Fig. S15, ESI†). However, scaling up the array size would necessitate the incorporation of selection devices to mitigate sneak path issues.[94] Furthermore, input images comprising the acronym of our laboratory 'O,' 'N,' 'N,' and 'L' in a 3 × 3-pixel format were encoded (as shown in Fig. 7(d)). The resulting output current of these letters is presented in Fig. 7(e). The letter bitmap images were effectively stored and retrieved by the crossbar array. This successful demonstration of the 3 × 3 crossbar array highlights the practical applicability of the FCPI-SCN device, thereby showcasing its promising potential in advanced memory technologies. Despite the significant challenges associated with device scaling, including process compatibility and precise thickness control of the halide layer, many efforts are currently underway. First of all, halide perovskite films exhibit vulnerabilities when exposed to polar solvents such as acetone and water, which are commonly used in semiconductor manufacturing processes. Addressing this limitation is imperative for the practical deployment of halide perovskite-based resistive switching memory. Recent studies suggest that exploiting solvent orthogonality can be an effective strategy for adapting lithography techniques to halide perovskites.[15,95] Notably, halide perovskite films remain undamaged when exposed to nonpolar and weakly polar solvents, including chlorobenzene, hexane, and isopropanol. Additionally,

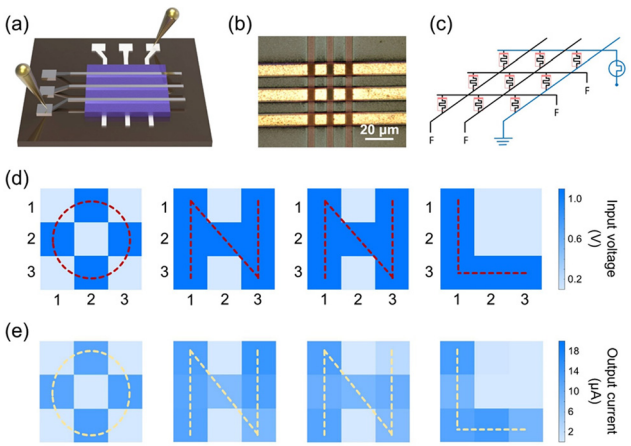

Fig. 7 Demonstration of crossbar array with Ag/PMMA/FCPI-SCN/Pt devices. (a) Schematic and (b) optical image of the 3 × 3 crossbar array. (c) Simplified equivalent circuit for the V_r scheme. (d) 3 × 3-pixel voltage input encoded in the letter shapes of 'O,' 'N,' 'N,' and 'L.' (e) Output current with the pattern of the letters 'O,' 'N,' 'N,' and 'L'.

Open Access Article. Published on 10 April 2025. Downloaded on 8/1/2025 4:22:04 PM. This article is licensed under a Creative Commons Attribution-NonCommercial 3.0 Unported Licence.

the thermal evaporation of halide-based sources can facilitate precise thickness control of halide perovskite films, enabling the fabrication of ultra-thin layers in large-scale wafer production.[96,97] In the context of large-scale array fabrication, the challenge of leakage current remains unresolved. Recent studies have suggested that threshold switching memristors are suitable as selector devices in 1-selector-1-resistor (1S-1R) memristor arrays.[98] Halide perovskite-based threshold switching devices have demonstrated low operating voltage and high selectivity.[99,100] Employing identical material systems for both the selector and the resistor could enhance process efficiency. The next step should involve investigating the integration of these films to achieve 1S-1R operation. The progress made in halide perovskite-based memory technologies demonstrates their substantial potential for future electronics.

Conclusions

In summary, our objective was to develop a low-powered filamentary memristor device based on mixed-cation HPs, specifically focusing on $FA_{0.8}Cs_{0.2}PbI_3$. By incorporating thiocyanate treatment, we successfully stabilized the cubic α-phase, leading to notable improvements in nonvolatile characteristics, such as enhanced retention and endurance. The pristine FCPI exhibits a mixed state of α and δ-phases, with heterostructures containing a high density of defects. These defects act as electron traps at the defective boundaries, facilitating the formation of multiple dendritic Ag thin filaments along the heterostructures and contributing to the fast corrosion of the filaments and unstable nonvolatile performance observed in the pristine FCPI. The reduction in the formation of the hexagonal δ-phase by-product and stabilization of cubic α-phase within FCPI-SCN substantially enhanced device performances. The Ag/PMMA/FCPI-SCN/Pt device exhibited a prolonged retention time of 1.1×10^4 s and improved endurance up to 1200 cycles. Additionally, the device could be programmed into six distinct multilevel resistance states. We also implemented a 3×3 crossbar array utilizing FCPI-SCN, which successfully encoded 3×3-pixel bitmaps representing various letters, such as 'O,' 'N,' 'N,' and 'L.' These bitmaps were reliably retained, showcasing their practical applicability for dependable resistive switching memory. In addition to elucidating the filamentary switching mechanisms, this work represents a significant step forward in the development of mixed-cation HP-based filamentary memristor devices, demonstrating the potential of novel functional materials for next-generation memory technologies. Our research opens new avenues for exploring and utilizing HPs in the realm of CBRAM.

Data availability

The data supporting the findings of this study are available within this article and its ESI,† or from the corresponding authors upon request.

Conflicts of interest

There are no conflicts to declare.

Acknowledgements

This work was financially supported by National R&D Program (RS-2024-00405016 and RS-2024-00404254) through NRF (National Research Foundation of Korea), funded by the Ministry of Science and ICT. The Research Institute of Advanced Materials, Inter-University Semiconductor Research Center, SOFT Foundry, and Institute of Engineering Research at Seoul National University provided research facilities for this work.

References

1 Z. Wang, H. Wu, G. W. Burr, C. S. Hwang, K. L. Wang, Q. Xia and J. J. Yang, *Nat. Rev. Mater.*, 2020, **5**, 173–195.
2 J. J. Yang and R. S. Williams, *ACM J. Emerg. Technol. Comput. Syst.*, 2013, **9**, 1–20.
3 M. Di Ventra and Y. V. Pershin, *Nat. Phys.*, 2013, **9**, 200–202.
4 C. Sun, S. Okamoto, S. Hachiya, T. Yamada and K. Takeuchi, *IEEE Trans. Consum. Electron.*, 2016, **62**, 267–274.
5 D. B. Strukov, G. S. Snider, D. R. Stewart and R. S. Williams, *Nature*, 2008, **453**, 80–83.
6 I. Vourkas and G. C. Sirakoulis, *Memristor-Based Nanoelectronic Computing Circuits and Architectures*, 2015.
7 I. H. Im, S. J. Kim and H. W. Jang, *Adv. Intell. Syst.*, 2020, **2**, 2000105.
8 S. Pi, C. Li, H. Jiang, W. Xia, H. Xin, J. J. Yang and Q. Xia, *Nat. Nanotechnol.*, 2019, **14**, 35–39.
9 Z. Wang, S. Joshi, S. Savel'Ev, W. Song, R. Midya, Y. Li, M. Rao, P. Yan, S. Asapu, Y. Zhuo, H. Jiang, P. Lin, C. Li, J. H. Yoon, N. K. Upadhyay, J. Zhang, M. Hu, J. P. Strachan, M. Barnell, Q. Wu, H. Wu, R. S. Williams, Q. Xia and J. J. Yang, *Nat. Electron.*, 2018, **1**, 137–145.
10 Y.-W. Song, J. Lee, S. Lee, W. Ham, J. H. Yoon, J.-M. Park, T. Sung and J.-Y. Kwon, *Electron. Mater. Lett.*, 2024, **20**, 725–732.
11 B. K. You, J. M. Kim, D. J. Joe, K. Yang, Y. Shin, Y. S. Jung and K. J. Lee, *ACS Nano*, 2016, **10**, 9478–9488.
12 H. Gim, M. Lee, W. Hong and K. Hong, *The Korean Sensors Society*, 2024, preprint, DOI: **10.46670/JSST.2024.33.5.265**.
13 L. Wang and J. Choi, *Micro Nano Syst. Lett.*, 2023, **11**, 5.
14 B. G. Lee, J.-Y. Lee, J. H. Choi, J. M. Seo and S.-J. Kim, *Electron. Mater. Lett.*, 2025, DOI: **10.1007/s13391-025-00555-x**.
15 J. Choi, J. S. Han, K. Hong, S. Y. Kim and H. W. Jang, *Adv. Mater.*, 2018, **30**, 1704002.
16 H. M. Cho and H. W. Jang, *Electron. Mater. Lett.*, 2025, DOI: **10.1007/s13391-025-00560-0**.
17 M. Kerara, A. Naas, A. Gueddim and O. Meglali, *Trans. Electr. Electron. Mater.*, 2024, **25**, 665–673.
18 A. Jabar, S. Benyoussef and L. Bahmad, *Trans. Electr. Electron. Mater.*, 2024, **25**, 519–528.

 This journal is © The Royal Society of Chemistry 2025

Open Access Article. Published on 10 April 2025. Downloaded on 8/1/2025 4:22:04 PM.
This article is licensed under a Creative Commons Attribution-NonCommercial 3.0 Unported Licence.

19 J. S. Han, Q. Van Le, J. Choi, K. Hong, C. W. Moon, T. L. Kim, H. Kim, S. Y. Kim and H. W. Jang, *Adv. Funct. Mater.*, 2018, **28**, 1705783.
20 J. S. Han, Q. Van Le, H. Kim, Y. J. Lee, D. E. Lee, I. H. Im, M. K. Lee, S. J. Kim, J. Kim, K. J. Kwak, M. J. Choi, S. A. Lee, K. Hong, S. Y. Kim and H. W. Jang, *Small*, 2020, **16**, 2003225.
21 S. J. Kim, T. H. Lee, J. M. Yang, J. W. Yang, Y. J. Lee, M. J. Choi, S. A. Lee, J. M. Suh, K. J. Kwak, J. H. Baek, I. H. Im, D. E. Lee, J. Y. Kim, J. Kim, J. S. Han, S. Y. Kim, D. Lee, N. G. Park and H. W. Jang, *Mater. Today*, 2022, **52**, 19–30.
22 J. Choi, S. Park, J. Lee, K. Hong, D. H. Kim, C. W. Moon, G. Do Park, J. Suh, J. Hwang, S. Y. Kim, H. S. Jung, N. G. Park, S. Han, K. T. Nam and H. W. Jang, *Adv. Mater.*, 2016, **28**, 6562–6567.
23 J. Choi, Q. Van Le, K. Hong, C. W. Moon, J. S. Han, K. C. Kwon, P. R. Cha, Y. Kwon, S. Y. Kim and H. W. Jang, *ACS Appl. Mater. Interfaces*, 2017, **9**, 30764–30771.
24 S. Poddar, Y. Zhang, L. Gu, D. Zhang, Q. Zhang, S. Yan, M. Kam, S. Zhang, Z. Song, W. Hu, L. Liao and Z. Fan, *Nano Lett.*, 2021, **21**, 5036–5044.
25 K. C. Kwon, K. Hong, Q. Van Le, S. Y. Lee, J. Choi, K. B. Kim, S. Y. Kim and H. W. Jang, *Adv. Funct. Mater.*, 2016, **26**, 4213–4222.
26 S. H. Turren-Cruz, A. Hagfeldt and M. Saliba, *Science*, 1979, **2018**(362), 449–453.
27 B. Conings, J. Drijkoningen, N. Gauquelin, A. Babayigit, J. D'Haen, L. D'Olieslaeger, A. Ethirajan, J. Verbeeck, J. Manca, E. Mosconi, F. De Angelis and H. G. Boyen, *Adv. Energy Mater.*, 2015, **5**, 1500477.
28 J. W. Lee, D. H. Kim, H. S. Kim, S. W. Seo, S. M. Cho and N. G. Park, *Adv. Energy Mater.*, 2015, **5**, 1501310.
29 D. Ghosh, A. R. Smith, A. B. Walker and M. S. Islam, *Chem. Mater.*, 2018, **30**, 5194–5204.
30 S. S. W. S. Yang, J. Noh, Y. C. Kim, S. Ryu and J. Seo, *Science*, 2015, **348**, 1234–1237.
31 A. Binek, F. C. Hanusch, P. Docampo and T. Bein, *J. Phys. Chem. Lett.*, 2015, **6**, 1249–1253.
32 J. W. Lee, D. J. Seol, A. N. Cho and N. G. Park, *Adv. Mater.*, 2014, **26**, 4991–4998.
33 Z. Li, M. Yang, J. S. Park, S. H. Wei, J. J. Berry and K. Zhu, *Chem. Mater.*, 2016, **28**, 284–292.
34 J. S. Yun, J. Kim, T. Young, R. J. Patterson, D. Kim, J. Seidel, S. Lim, M. A. Green, S. Huang and A. Ho-Baillie, *Adv. Funct. Mater.*, 2018, **28**, 1705363.
35 S. Tan, I. Yavuz, M. H. Weber, T. Huang, C. H. Chen, R. Wang, H. C. Wang, J. H. Ko, S. Nuryyeva, J. Xue, Y. Zhao, K. H. Wei, J. W. Lee and Y. Yang, *Joule*, 2020, **4**, 2426–2442.
36 X. Zhao, J. Ma, X. Xiao, Q. Liu, L. Shao, D. Chen, S. Liu, J. Niu, X. Zhang, Y. Wang, R. Cao, W. Wang, Z. Di, H. Lv, S. Long and M. Liu, *Adv. Mater.*, 2018, **30**, 1705193.
37 M. J. Lee, S. Han, S. H. Jeon, B. H. Park, B. S. Kang, S. E. Ahn, K. H. Kim, C. B. Lee, C. J. Kim, I. K. Yoo, D. H. Seo, X. S. Li, J. B. Park, J. H. Lee and Y. Park, *Nano Lett.*, 2009, **9**, 1476–1481.
38 H. Kim, J. S. Kim, J. Choi, Y. H. Kim, J. M. Suh, M. J. Choi, Y. S. Shim, S. Y. Kim, T. W. Lee and H. W. Jang, *ACS Appl. Mater. Interfaces*, 2024, **16**, 2457–2466.
39 C. Muthu, A. N. Resmi, A. Ajayakumar, N. E. A. Ravindran, G. Dayal, K. B. Jinesh, K. Szaciłowski and C. Vijayakumar, *Small*, 2024, **20**, 1–12.
40 S. M. Lee, H. Kim, D. H. Kim, W. Bin Kim, J. M. Lee, J. Choi, H. Shin, G. S. Han, H. W. Jang and H. S. Jung, *ACS Appl. Mater. Interfaces*, 2020, **12**, 17039–17045.
41 C. Eames, J. M. Frost, P. R. F. Barnes, B. C. O'Regan, A. Walsh and M. S. Islam, *Nat. Commun.*, 2015, **6**, 7497.
42 J. S. Han, Q. Van Le, J. Choi, K. Hong, C. W. Moon, T. L. Kim, H. Kim, S. Y. Kim and H. W. Jang, *Adv. Funct. Mater.*, 2018, **28**, 1705783.
43 M. L. Holekevi Chandrappa, Z. Zhu, D. P. Fenning and S. P. Ong, *Chem. Mater.*, 2021, **33**, 4672–4678.
44 D. Y. Heo, T. H. Lee, A. Iwan, L. Kavan, M. Omatova, E. Majkova, K. Kamarás, H. W. Jang and S. Y. Kim, *J. Power Sources*, 2020, **458**, 228067.
45 Y. Chen, B. Li, W. Huang, D. Gao and Z. Liang, *Chem. Commun.*, 2015, **51**, 11997–11999.
46 A. Halder, R. Chulliyil, A. S. Subbiah, T. Khan, S. Chattoraj, A. Chowdhury and S. K. Sarkar, *J. Phys. Chem. Lett.*, 2015, **6**, 3483–3489.
47 Q. Jiang, D. Rebollar, J. Gong, E. L. Piacentino, C. Zheng and T. Xu, *Angew. Chem., Int. Ed.*, 2015, **54**, 7617–7620.
48 Y. Yu, C. Wang, C. R. Grice, N. Shrestha, J. Chen, D. Zhao, W. Liao, A. J. Cimaroli, P. J. Roland, R. J. Ellingson and Y. Yan, *ChemSusChem*, 2016, **9**, 3288–3297.
49 L. T. Schelhas, Z. Li, J. A. Christians, A. Goyal, P. Kairys, S. P. Harvey, D. H. Kim, K. H. Stone, J. M. Luther, K. Zhu, V. Stevanovic and J. J. Berry, *Energy Environ. Sci.*, 2019, **12**, 1341–1348.
50 G. Kieslich, S. Sun and A. K. Cheetham, *Chem. Sci.*, 2015, **6**, 3430–3433.
51 M. Abdi-Jalebi, Z. Andaji-Garmaroudi, S. Cacovich, C. Stavrakas, B. Philippe, J. M. Richter, M. Alsari, E. P. Booker, E. M. Hutter, A. J. Pearson, S. Lilliu, T. J. Savenije, H. Rensmo, G. Divitini, C. Ducati, R. H. Friend and S. D. Stranks, *Nature*, 2018, **555**, 497–501.
52 D. Y. Son, S. G. Kim, J. Y. Seo, S. H. Lee, H. Shin, D. Lee and N. G. Park, *J. Am. Chem. Soc.*, 2018, **140**, 1358–1364.
53 S. Yang, W. Liu, L. Zuo, X. Zhang, T. Ye, J. Chen, C. Z. Li, G. Wu and H. Chen, *J. Mater. Chem. A*, 2016, **4**, 9430–9436.
54 R. Waser, R. Dittmann, C. Staikov and K. Szot, *Adv. Mater.*, 2009, **21**, 2632–2663.
55 S. Aussen, F. Cüppers, C. Funck, J. Jo, S. Werner, C. Pratsch, S. Menzel, R. Dittmann, R. Dunin-Borkowski, R. Waser and S. Hoffmann-Eifert, *Adv. Electron. Mater.*, 2023, **9**, 2300520.
56 W. Banerjee, W. F. Cai, X. Zhao, Q. Liu, H. Lv, S. Long and M. Liu, *Nanoscale*, 2017, **9**, 18908–18917.
57 C. C. Hsieh, A. Roy, A. Rai, Y. F. Chang and S. K. Banerjee, *Appl. Phys. Lett.*, 2015, **106**, 173108.
58 H. F. Ling, M. D. Yi, M. Nagai, L. H. Xie, L. Y. Wang, B. Hu and W. Huang, *Adv. Mater.*, 2017, **29**, 1–9.

Open Access Article. Published on 10 April 2025. Downloaded on 8/1/2025 4:22:04 PM. This article is licensed under a Creative Commons Attribution-NonCommercial 3.0 Unported Licence.

59 M. A. Lampert and R. B. Schilling, *Chapter 1 Current Injection in Solids: The Regional Approximation Method*, 1970, pp. 1–96.
60 Y. C. Yang, F. Pan, Q. Liu, M. Liu and F. Zeng, *Nano Lett.*, 2009, **9**, 1636–1643.
61 D. Meggiolaro, E. Mosconi and F. De Angelis, *ACS Energy Lett.*, 2019, **4**, 779–785.
62 P. Calado, A. M. Telford, D. Bryant, X. Li, J. Nelson, B. C. O'Regan and P. R. F. Barnes, *Nat. Commun.*, 2016, **7**, 1–10.
63 Z. Fang, W. Chen, Y. Shi, J. Zhao, S. Chu, J. Zhang and Z. Xiao, *Adv. Funct. Mater.*, 2020, **30**, 1–9.
64 A. S. Thind, X. Huang, J. Sun and R. Mishra, *Chem. Mater.*, 2017, **29**, 6003–6011.
65 J. S. Yun, J. Kim, T. Young, R. J. Patterson, D. Kim, J. Seidel, S. Lim, M. A. Green, S. Huang and A. Ho-Baillie, *Adv. Funct. Mater.*, 2018, **28**, 1705363.
66 S. Tan, I. Yavuz, M. H. Weber, T. Huang, C. H. Chen, R. Wang, H. C. Wang, J. H. Ko, S. Nuryyeva, J. Xue, Y. Zhao, K. H. Wei, J. W. Lee and Y. Yang, *Joule*, 2020, **4**, 2426–2442.
67 W. Yang, S. Lee, H. C. Kwon, J. Tan, H. Lee, J. Park, Y. Oh, H. Choi and J. Moon, *ACS Nano*, 2018, **12**, 11088–11097.
68 X. Song, W. Wang, P. Sun, W. Ma and Z. K. Chen, *Appl. Phys. Lett.*, 2015, **106**, 033901.
69 A. Dehingia, U. Das and A. Roy, *Mater. Today: Proc.*, 2022, **65**, 29–34.
70 H. Du, C. L. Jia, A. Koehl, J. Barthel, R. Dittmann, R. Waser and J. Mayer, *Chem. Mater.*, 2017, **29**, 3164–3173.
71 X. Xu, H. Lv, H. Liu, T. Gong, G. Wang, M. Zhang, Y. Li, Q. Liu, S. Long and M. Liu, *IEEE Electron Device Lett.*, 2015, **36**, 129–131.
72 W. Wang, M. Wang, E. Ambrosi, A. Bricalli, M. Laudato, Z. Sun, X. Chen and D. Ielmini, *Nat. Commun.*, 2019, **10**, 81.
73 S. A. Chekol, S. Menzel, R. W. Ahmad, R. Waser and S. Hoffmann-Eifert, *Adv. Funct. Mater.*, 2022, **32**, 2111242.
74 Q. Jiang, D. Rebollar, J. Gong, E. L. Piacentino, C. Zheng and T. Xu, *Angew. Chem., Int. Ed.*, 2015, **54**, 7617–7620.
75 I. H. Im, J. H. Baek, S. J. Kim, J. Kim, S. H. Park, J. Y. Kim, J. J. Yang and H. W. Jang, *Adv. Mater.*, 2024, **36**, 1–13.
76 S. Paramanik and A. J. Pal, *Adv. Electron. Mater.*, 2022, **8**, 2200211.
77 T. H. Park, H. J. Kim, W. Y. Park, S. G. Kim, B. J. Choi and C. S. Hwang, *Nanoscale*, 2017, **9**, 6010–6019.
78 H. Schroeder, V. V. Zhirnov, R. K. Cavin and R. Waser, *J. Appl. Phys.*, 2010, **107**, 054517.
79 A. Gubicza, M. Csontos, A. Halbritter and G. Mihály, *Nanoscale*, 2015, **7**, 4394–4399.
80 P. Huang, Y. Wang, H. Li, B. Gao, B. Chen, F. Zhang, L. Zeng, G. Du, J. Kang and X. Liu, *IEEE Trans. Nanotechnol.*, 2014, **13**, 1127–1132.
81 B. G. Chae, J. B. Seol, J. H. Song, K. Baek, S. H. Oh, H. Hwang and C. G. Park, *Adv. Mater.*, 2017, **29**, 1701752.
82 R. A. John, Y. Demirağ, Y. Shynkarenko, Y. Berezovska, N. Ohannessian, M. Payvand, P. Zeng, M. I. Bodnarchuk, F. Krumeich, G. Kara, I. Shorubalko, M. V. Nair, G. A. Cooke, T. Lippert, G. Indiveri and M. V. Kovalenko, *Nat. Commun.*, 2022, **13**, 2074.
83 X. Yan, C. Qin, C. Lu, J. Zhao, R. Zhao, D. Ren, Z. Zhou, H. Wang, J. Wang, L. Zhang, X. Li, Y. Pei, G. Wang, Q. Zhao, K. Wang, Z. Xiao and H. Li, *ACS Appl. Mater. Interfaces*, 2019, **11**, 48029–48038.
84 J. Ryu, K. Park, D. P. Sahu and T. S. Yoon, *ACS Appl. Mater. Interfaces*, 2024, **16**, 26450–26459.
85 S. Gao, C. Chen, Z. Zhai, H. Y. Liu, Y. S. Lin, S. Z. Li, S. H. Lu, G. Y. Wang, C. Song, F. Zeng and F. Pan, *Appl. Phys. Lett.*, 2014, **105**, 063504.
86 J. Li, X. Zhou, L. Xu, J. Wang, B. Wu and C. Wang, *Mater. Res. Express*, 2022, **9**, 035003.
87 S. Munjal and N. Khare, *Nanotechnology*, 2021, **32**, 185204.
88 N. Ilyas, J. Wang, C. Li, H. Fu, D. Li, X. Jiang, D. Gu, Y. Jiang and W. Li, *J. Mater. Sci. Technol.*, 2022, **97**, 254–263.
89 D. P. Do, V. Q. Bui, M. C. Nguyen, S. Seo, V. D. Do, J. Kim, J. Choi, H. Ko, W. J. Yu, Y. Kawazoe and H. Lee, *Nano Lett.*, 2024, **24**, 7999–8007.
90 X. Feng, Y. Li, L. Wang, S. Chen, Z. G. Yu, W. C. Tan, N. Macadam, G. Hu, L. Huang, L. Chen, X. Gong, D. Chi, T. Hasan, A. V. Y. Thean, Y. W. Zhang and K. W. Ang, *Adv. Electron. Mater.*, 2019, **5**, 1–9.
91 M. K. Yadav, S. S. Kundale, S. S. Sutar, T. D. Dongale, P. Kumar and N. Panwar, *J. Appl. Phys.*, 2023, **134**, 105101.
92 S. Gao, C. Song, C. Chen, F. Zeng and F. Pan, *J. Phys. Chem. C*, 2012, **116**, 17955–17959.
93 J. Y. Seo, J. Choi, H. S. Kim, J. Kim, J. M. Yang, C. Cuhadar, J. S. Han, S. J. Kim, D. Lee, H. W. Jang and N. G. Park, *Nanoscale*, 2017, **9**, 15278–15285.
94 I. H. Im, S. J. Kim, J. H. Baek, K. J. Kwak, T. H. Lee, J. W. Yang, D. E. Lee, J. Y. Kim, H. R. Kwon, D. Y. Heo, S. Y. Kim and H. W. Jang, *Adv. Funct. Mater.*, 2022, **33**, 2211358.
95 C. H. Lin, B. Cheng, T. Y. Li, J. R. D. Retamal, T. C. Wei, H. C. Fu, X. Fang and J. H. He, *ACS Nano*, 2019, **13**, 1168–1176.
96 S. Y. Hsiao, H. L. Lin, W. H. Lee, W. L. Tsai, K. M. Chiang, W. Y. Liao, C. Z. Ren-Wu, C. Y. Chen and H. W. Lin, *Adv. Mater.*, 2016, **28**, 7013–7019.
97 L. Gil-Escrig, C. Momblona, M. G. La-Placa, P. P. Boix, M. Sessolo and H. J. Bolink, *Adv. Energy Mater.*, 2018, **8**, 1–6.
98 H. J. Kim, D. S. Woo, S. M. Jin, H. J. Kwon, K. H. Kwon, D. W. Kim, D. H. Park, D. E. Kim, H. U. Jin, H. Do Choi, T. H. Shim and J. G. Park, *Adv. Mater.*, 2022, **34**, 2203643.
99 L. Tang, J. Wang, Y. Huang, H. Wang, C. Wang and Y. Yang, *J. Mater. Chem. C*, 2024, **12**, 3622–3631.
100 I. H. Im, S. J. Kim, J. H. Baek, K. J. Kwak, T. H. Lee, J. W. Yang, D. E. Lee, J. Y. Kim, H. R. Kwon, D. Y. Heo, S. Y. Kim and H. W. Jang, *Adv. Funct. Mater.*, 2022, **33**, 2211358.

 This journal is © The Royal Society of Chemistry 2025